CrystEngComm

PAPER

View Article Online
View Journal | View Issue

Cite this: *CrystEngComm*, 2024, **26**, 4525

Effect of supramolecular complexation of alkali hydrogenselenates with crown ethers and solid-solutions with their hydrogensulfate counterparts on the solid-to-solid phase transition behaviors†

Samet Ocak,‡ Dario Braga and Simone d'Agostino *

This study investigates the structural and phase transition characteristics of supramolecular complexes composed of 18-crown-6 ether and hydrogen selenate ($HSeO_4^-$) anions with various cations (K^+, Rb^+, Cs^+). Single crystals of [18-crown-6·K]$HSeO_4$·$2H_2O$, [18-crown-6·Rb]$HSeO_4$·H_2O, [18-crown-6·Cs]$HSeO_4$·H_2O, [18-crown-6·K]$HSeO_4$, and [18-crown-6·K]$(HSeO_4)_{0.5}(HSO_4)_{0.5}$ were grown and their structures determined *via* single-crystal X-ray diffraction. Differential scanning calorimetry and variable-temperature powder X-ray diffraction were employed to analyse dehydration and phase transition behaviors. The inclusion of 18-crown-6 ether significantly lowered the superprotonic phase transition temperatures by approximately 40 °C compared to pure solid acids. Additionally, substituting HSO_4^- with $HSeO_4^-$ decreased phase transition temperatures for K and Cs-complexes and modified the phase transition behavior of the Rb-complex from two-step to single-step isostructural phase transition. Attempts to form solid solutions between the $HSeO_4^-$ and HSO_4^- complexes yielded mixed results, with notable success in modulating phase transition temperatures in K-complexes.

Received 21st May 2024,
Accepted 22nd July 2024

DOI: 10.1039/d4ce00514g

rsc.li/crystengcomm

Introduction

Solid electrolytes, which are known for their fast ion conduction, have attracted much attention in recent years for their various applications in electronic devices such as batteries, supercapacitors, molecular sensors, and fuel cells.[1–8] One example of a solid electrolyte is Nafion, an organic polymer that contains sulfonic acid residues. It has a conductivity range of 10^{-1} to 10^{-5} S cm^{-1}, which is affected by factors like temperature, hydration state, thermal history, and processing conditions.[9–15] Current research is, thus, focused on finding materials that can conduct protons at high temperatures (100–300 °C) in dry or anhydrous environments.[7,16–19] Many alternatives have been proposed, including polymers, metal–organic frameworks (MOFs), covalent organic frameworks (COFs), metal oxides, glasses, and plastic crystals (PCs), all of which have shown promising characteristics for proton conductivity.[5,11,16,18,20–32] Since they all have their pros and cons depending on different working conditions (temperature intervals, hydration levels, *etc.*), searching for alternative materials is still ongoing.

Solid acids with the chemical formulas $MHAO_4$ and MH_2BO_4, where M represents alkali cations, A represents S or Se, and B represents P or As, have been found to exhibit high protonic conductivity.[33,34] This is due to the presence of dynamically disordered hydrogen-bond networks associated with reversible first-order solid-to-solid transitions, which are referred to as superprotonic phase transitions.[2,35–40] Solid acids are more advantageous than polymeric electrolytes because they operate at higher temperatures, do not require humidification, and are impermeable to other ions or radical species thanks to their solid form.[41,42] Moreover, studies have shown that for solid acids proton conductivity is further enhanced in the presence of larger cations, such as Cs^+ compared to Rb^+ and K^+.[37,43] In general, the crystal lattice of alkali hydrogen sulfates and selenates undergoes significant structural changes at high temperatures resulting in a solid-to-solid transition associated with an increase in crystal symmetry, and generation of dynamic disorder of the H-bond network, causing both protons and H-bonds to be de-localized over the entire lattice. Proton conduction in these crystals occurs through a structure diffusion mechanism, known as the Grotthuss mechanism,[44] and are termed superprotonic phases.[35,45] The hydrogen selenates can be expected to be more advantageous than the hydrogen sulfates because their

The University of Bologna – Department of Chemistry "Giacomo Ciamician", Via F. Selmi 2, 40126, Bologna (BO), Italy

† Electronic supplementary information (ESI) available: DSC traces, VT-PXRD results and crystallographic information. CCDC 2350122–2350126. For ESI and crystallographic data in CIF or other electronic format see DOI: **https://doi.org/10.1039/d4ce00514g**

‡ Current address: Institute for Microelectronics and Microsystems - Research National Council (IMM-CNR), *Via* Pietro Gobetti 101, 40129, Bologna (BO), Italy.

superprotonic phase transitions take place at lower temperatures (see below).[37,46,47]

In our previous work,[46] we discussed how the crystal structure of supramolecular complexes, comprising 18-crown-6 as the ligand and either potassium or rubidium as the cations, alongside hydrogen sulfate as the anion, influence their superprotonic conduction properties. These compounds were found to undergo enantiotropic solid-to-solid transitions associated with the onset of a dynamical process affecting both the crown ether ligand and the hydrogensulfate anion.

Our goal in advancing the search for new materials capable in conducting small ions such as protons entails merging the principles of Crystal Engineering[48–50] with solid-solution formation techniques,[51,52] to craft a versatile molecular toolkit for creating crystalline solids that exhibit phase transitions at varying temperatures.[53–55]

The aim of the work presented herein was essentially twofold. First, we were interested in investigating the impact of a different anion, specifically hydrogen selenate ($HSeO_4^-$), while using Cs^+, Rb^+, and K^+ as the cations hosted in the cavity of 18-crown-6 ether. Crown ethers exhibit a pronounced affinity for alkali metal cations whose ionic radii align with the dimensions of their binding cavities, defined by the surrounding O-atoms.[56,57] As a matter of fact, 18-crown-6 demonstrates a distinct preference for binding with K^+; though, on passing to the larger cations such as Rb^+ and Cs^+, it can still form complexes, albeit with a reduced binding affinity. As a result, K^+ seamlessly accommodates itself within, whereas Rb^+ and Cs^+ ions, depicted in Scheme 1a, position themselves above the midplane established by the crown ether molecule, extending beyond the cavities according to the ionic radii, and leaving larger cations partly "naked". These cations must inevitably engage O-atoms from anions or water molecules to fulfill their coordination sphere. This is expected to influence metal coordination significantly and will shape the resulting crystalline materials' distinctive structural, thermal, and conduction characteristics.

Second, we wanted to explore the possibility of preparing crystalline solid solutions with their hydrogensulfate analogs (Scheme 1b) and studying how the composition of the resulting materials further affects the phase transition compared to the pure parent systems.

To achieve these objectives, we have grown single crystals of the supramolecular complexes made up of 18-crown-6 and $MHSeO_4$ (where $M^+ = K^+$, Rb^+, Cs^+). Subsequently, we employed single-crystal X-ray diffraction data to elucidate their structures, thereby discerning the distinctive structural variations induced by diverse cations. The determined structures were identified as 18-crown-6·$KHSeO_4$·$2H_2O$ (**1**·$2H_2O$), 18-crown-6·$RbHSeO_4$·H_2O (**2**·H_2O), and 18-crown-6·$CsHSeO_4$·H_2O (**3**·H_2O). Next, we have used the differential scanning calorimetry (DSC) technique to explore their dehydration and phase transition behaviors which in general could be summarized as:

$$\text{HYDRATED COMPLEX} \rightleftharpoons \text{ANHYDROUS COMPLEX} \rightleftharpoons \text{HT ANHYDROUS COMPLEX.}$$

Variable-temperature powder XRD was essential to further analyse and confirm the DSC results. It was observed that the superprotonic phase transition temperatures were significantly decreased upon formation of the assembly of 18-crown-6 ether into the structure compared to the pure solid acids. While the phase transition temperature decreased significantly from **1** to **3**, the Rb-complex **2** showed an isostructural phase transition that occurs at higher temperatures than the other two compounds in the series. On the other hand, replacing HSO_4^- (ref. 46) with $HSeO_4^-$ caused a decrease in the phase transition temperature of K-complexes while changing the Rb-complex's behavior entirely. Finally, given the high degree of isomorphism and isostructurality of the novel $HSeO_4^-$ supramolecular complexes with their HSO_4^- counterparts, we also attempted solid-solution[51,52] formation to achieve mixed phases with modulated phase transition behaviors.

Experimental

Synthesis

$KHSeO_4$, $RbHSeO_4$, and $CsHSeO_4$ were synthesized by combining related alkali metal carbonate salt, *i.e.*, K_2CO_3 (Sigma-

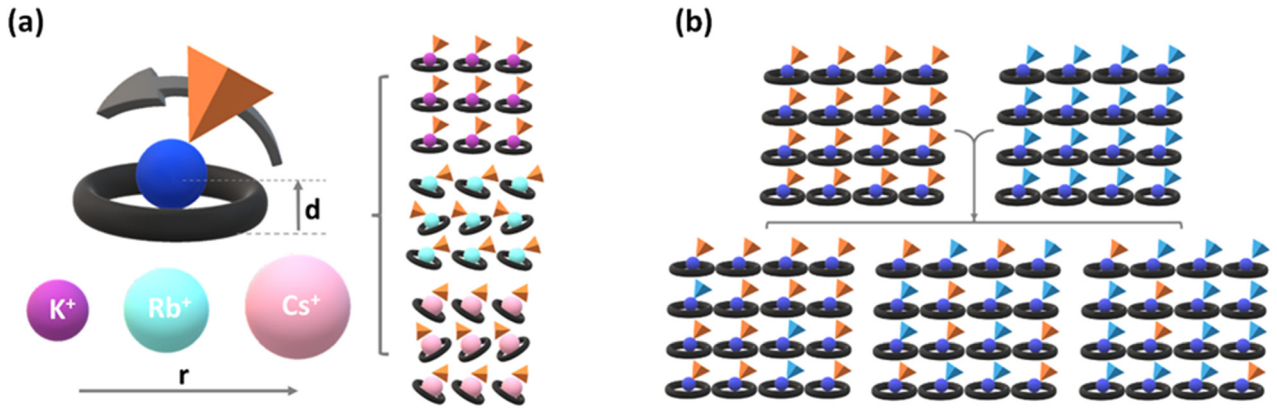

Scheme 1 (a) Representation showing how the alkali cation (blue sphere) fits inside the 18-crown-6 ether cavity (black ring), remaining "naked" to the extent of their sizes. Distance (*d*) is expected to increase with cationic radius, and (b) general scheme for solid solution formation; orange and blue tetrahedra represent $HSeO_4^-$ and HSO_4^- anions, respectively.

Aldrich ≥98%), Rb_2CO_3 (Sigma-Aldrich ≥98%), and Cs_2CO_3 (Merck ≥99%) with an excess amount of H_2SeO_4 (40 wt% in H_2O, 99.95%) dissolved in water. The hydrogen selenate crystals were grown after approximately 2 days. The resulting crystals were filtered and subsequently washed with methanol. Then, they were dissolved again in the water together with a slight excess amount of 18-crown-6 (*ca.* 1.2 equivalents) to synthesize the hydrated supramolecular crown complex of each salt. After slow evaporation, the resulting crystals were washed with octane to remove the excess 18-crown-6 ether. In order to grow anhydrous single crystals of 18-crown-6·$KHSeO_4$, the hydrated complex is left in the oven for 3 hours at 80 °C and then dissolved in dry acetone and left in a desiccator. The single crystals of solid solution 18-crown-6·$K(HSO_4)_{0.5}(HSeO_4)_{0.5}$ were formed by dissolving the same stoichiometric amounts of anhydrous 18-crown-6·$KHSeO_4$ and 18-crown-6·$KHSO_4$ in dry acetone which was then left in the desiccator. The powder-formed solid solutions in all ranges of molecular fractions for all the complexes were prepared by hand grinding the appropriate amount of parent compounds.

X-Ray diffraction

The single-crystal data for 18-crown-6·$KHSeO_4$·$2H_2O$, 18-crown-6·$RbHSeO_4$·H_2O, 18-crown-6·$CsHSeO_4$·H_2O, 18-crown-6·$KHSeO_4$, and 18-crown-6·$K(HSO_4)_{0.5}(HSeO_4)_{0.5}$ were obtained using an Oxford X'Calibur S CCD diffractometer with a graphite monochromator. The diffractometer used Mo-Kα radiation with a wavelength of 0.71073 Å and an Oxford CryoStream800 cryostat. Twinning was observed in each crystal, and the reflection data were integrated using the default configuration for twinned crystals in the CrysAlisPro Software. The subsequent structural solution and refinement processes were conducted using the HKLF4 file, which included non-overlapping reflections. The structural solutions were obtained through intrinsic phasing using SHELXT[58] and subsequently refined on F^2 with SHELXL.[59] The refinement method used was the full-matrix least-squares refinement method within the Olex2 software.[60] The position of $H_{HSeO_4^-}$ atoms was either directly determined or inserted at calculated positions. H_{CH} atoms associated with all compounds were introduced at calculated positions and refined while riding on their respective carbon atoms. Anisotropic refinement was applied to all non-hydrogen atoms, accompanied by the implementation of rigid-body RIGU restraints.[61]

To identify phases and investigate variable-temperature behavior, powder X-ray diffractograms were obtained within the 2θ range of 5–40°. This was done using a Panalytical X'Pert PRO automated diffractometer equipped with an X'Celerator detector and operated in Bragg–Brentano geometry. The diffractometer used Cu Kα radiation without a monochromator. The step size was 0.02°, time per step was 20 s, the 0.04 rad soller was used and the operating current was 40 mA × 40 kV. All powder diffraction patterns of the hydrated forms were compared with the calculated patterns for controlling the purity of the bulk samples (Fig. ESI-1†).

Differential scanning calorimetry

Differential Scanning Calorimetry (DSC) analyses were performed on 18-crown-6·$KHSeO_4$·$2H_2O$, and 18-crown-6·$RbHSeO_4$·H_2O using a PerkinElmer DSC-7 instrument, equipped with a PII intracooler. Additionally, DSC measurements for 18-crown-6·$CsHSeO_4$·H_2O and all the solid solutions were carried out using a Q10 instrument from TA Instruments, fitted with a Refrigerated Cooling System (RCS90, TA instruments). The samples, with weights ranging between 3–5 mg, were heated in aluminum pans at a rate of 5 °C min^{-1} within the temperature range of 30–160 °C under a nitrogen (N_2) atmosphere.

Results and discussion

In the following sections, we present the structures, as determined from single-crystal analysis, of three hydrated supramolecular complexes: [18-crown-6·K]$HSeO_4$·$2H_2O$ (**1**·$2H_2O$), [18-crown-6·Rb]$HSeO_4$·H_2O (**2**·H_2O), [18-crown-6·Cs]$HSeO_4$·H_2O (**3**·H_2O). Subsequently, we analyse and discuss their dehydration and phase transition behaviors associated with increasing temperature, employing Differential Scanning Calorimetry (DSC) and variable-temperature powder X-ray diffraction (PXRD) analyses. Finally, we discuss our findings about solid solution formation with their hydrogensulfate analogous and present the structures of the anhydrous form of the K-complex, [18-crown-6·K]$HSeO_4$, and its solid solution [18-crown-6·K]$(HSeO_4)_{0.5}(HSeO_4)_{0.5}$.

Hydrated complexes

All compounds crystallize in the monoclinic system (see Table ESI-1† for details) with the metal cations coordinated by the crown ether. In compounds **1**·$2H_2O$ and **2**·H_2O, the coordination spheres are satisfied by two and three O-atoms originating from the hydrogenselenate anions, respectively. In the case of **3**·H_2O, an extra water molecule contributes to the coordination of the cesium cation, and, as expected, M^+ cations protrude above the midplane of the crown ether molecule according to their growing ionic radii (K^+ = 151 pm, Rb^+ = 161 pm, and Cs^+ = 167 pm). See Fig. 1 and Table 1 for distances. Due to the different coordination geometry, the $HSeO_4^-$ anions form hydrogen-bonded dimers, either among themselves or mediated by water molecules. **1**·$2H_2O$ is characterized by the presence of chains of $HSeO_4^-$ anions linked by hydrogen bonds *via* the water molecules to form supramolecular tapes [$O–H_w\cdots O_{HSeO_4^-}$ = 2.60(1)–2.79(1) Å and $O–H_w\cdots O_w$ = 2.70(1) Å], as depicted in Fig. 2a.

On the other hand, **2**·H_2O features hydrogen bonded $HSeO_4^-$ pairs [$O–H_{HSeO_4^-}\cdots O_{HSeO_4^-}$ = 2.601(5) Å] connecting two $[18\text{-crown-6·Rb}]^+$ cationic units to form supramolecular dimers (Fig. 2b) which, in turn, are bridged *via* hydrogen bonds with water molecules [$O–H_w\cdots O_{HSeO_4^-}$ = 2.875(8) Å], whereas, in **3**·H_2O, the water molecule, unlike its counterparts in the series, directly coordinates with the alkali metal ion captured within the crown ether ring, as illustrated in Fig. 1. Furthermore, water molecules establish hydrogen

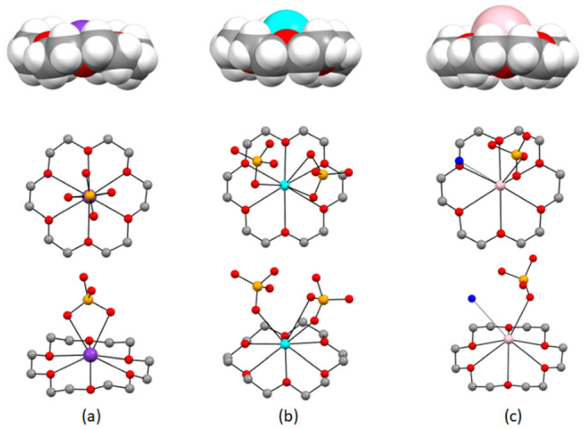

Fig. 1 Space filling representation showing the protrusion of the cations, according to their ionic radii, from the crown ether, and top and side views showing the coordination geometry of the around the K^+, Rb^+, and Cs^+ ions in crystalline **1**·2H_2O (a), **2**·H_2O (b), and **3**·H_2O (c). H-atoms omitted for clarity.

bonds with the oxygen atoms of the anions [$O–H_w\cdots O_{HSeO_4^-}$ = 2.74(3) Å], which also engage in interactions with each other, leading to the formation of a hydrogen-bonded supramolecular dimer [$O_{HSeO_4^-}\cdots O_{HSeO_4^-}$ = 2.64(3) Å], as depicted in Fig. 2c. The thermal characteristics of all complexes were examined through a combination of differential scanning calorimetry (DSC) and variable-temperature X-ray powder diffraction (VT-XRPD). DSC measurements for **1**·2H_2O, shown in Fig. ESI-2,† indicate that the complex undergoes dehydration at around 60 °C followed by a reversible solid-to-solid phase transition at 96 °C, with 19 °C hysteresis. The VT-PXRD experiments shown in Fig. 3 also confirm this. Fig. ESI-3† reveals that the powder diffractograms of [18-crown-6·K]$HSeO_4$ and [18-crown-6·K]HSO_4 exhibit striking similarity post-dehydration and after the solid-to-solid phase transition. This observation suggests that both compounds behave similarly from a structural standpoint. However, the replacement of HSO_4^- with $HSeO_4^-$ seems to be responsible for a decrease of approximately 20 °C in the phase transition temperature, which is noteworthy.

2·H_2O also experiences dehydration in the temperature range of 60–80 °C, as evidenced by Differential Scanning Calorimetry (DSC) measurements (Fig. ESI-4†). Subsequently, a reversible solid-to-solid phase transition occurs at approximately 125 °C. The structural transformations associated with these phenomena are closely monitored through variable-temperature powder XRD, as depicted in Fig. 3. It is noticeable that the dehydration process results in a clear change of peak positions from RT to 100 °C. However, the neat phase change is not observed at 125 °C. The broadening of diffraction peaks, and the lowering of their intensities are most consistent with an isostructural phase transition, which likely results in a higher level of mobility within the structure above 125 °C. Fig. ESI-5† shows a comparison of the powder diffractograms of rubidium HSO_4^- and $HSeO_4^-$ complexes in each phase. Although the structures are not isomorphous in their hydrated forms, they become isomorphous in their anhydrous and high temperature phases.

Furthermore, the DSC (Fig. SI-6†) and VT-PXRD (Fig. SI-7†) measured on **3**·H_2O show two non-resolved processes, occurring at 76 and 86 °C, likely associated with dehydration followed by a solid-to-solid transition. These results suggest that the specific position of the water molecule, *i.e.*, directly bound to the metal ion, is the main factor in stabilizing the structure. Finally, at around 140 °C, there is an endothermic peak belonging to the 18-crown-6 ether leaving the structure that is also confirmed by the VT-PXRD. This can be seen through the similarities in the powder pattern with the high-temperature phase of its Rb analogous (Fig. ESI-7†). On the other hand, unlike the other two selenate complexes in this series, **3**·H_2O has certain structural differences from its hydrogensulfate analogous[43] as shown in Fig. ESI-7.† Compared to the parent compounds $MHSeO_4$ (where M^+ = K^+, Rb^+, and Cs^+), the significant decrease in the solid-to-solid transition temperatures leading to superprotonic phases, as depicted in Table 2, can be attributed to both the supramolecular interactions weakening, *i.e.*, breaking and formation of hydrogen bonds arising from re-orientational motions of the $HSeO_4^-$ and the dynamic behavior affecting the 18-crown-6 ether ring. Also, the solid-to-solid phase transition behaviors are different in comparison to their hydrogensulfate counterparts. For K-complexes, the transition temperature is reduced from 116 °C (ref. 62) to 96 °C, and for Cs-complexes, it is changed from 90 °C (ref. 63) to 86 °C. In the sulfate counterpart of Rb-complex, it was a two-step first-order transition (116–122 °C);[46] in the selenate counterpart, it became a one-step isostructural phase transition.

It is worth noting that rehydration in this class of compounds occurs quite rapidly; when exposed to open air, they readily absorb water from the moisture in a matter of minutes.

Solid solutions

Finally, given the high degree of isomorphism and/or isostructurality of the novel $HSeO_4^-$ supramolecular complexes

Table 1 Coordination distances detected within crystalline **1**·2H_2O, **2**·H_2O, and **3**·H_2O

M^+	d^a (Å)	$M^+\cdots O_{crown}$ (Å)	$M^+\cdots O_{HSeO_4^-}$ (Å)	$M^+\cdots O_{water}$ (Å)
K^+	0.694(1)	2.772(7)–2.976(7)	2.901(9)–2.932(7)	—
Rb^+	1.098(2)	2.927(5)–3.044(3)	3.094(3)–3.297(4)	—
Cs^+	1.506(1)	3.075(9)–3.25(1)	3.19(1)	3.67(2)

[a] Distance between the metal cation M^+ and the midplane of the crown ether ligand as defined in Scheme 1.

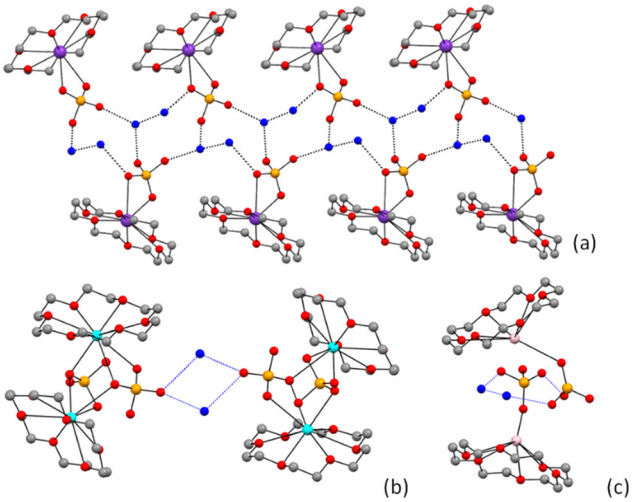

Fig. 2 Hydrogen bond patterns detected within crystalline: (a) **1**·2H_2O, (b) **2**·H_2O, and (c) **3**·H_2O. Water molecules in blue and H-atoms were omitted for clarity.

with their HSO_4^- counterparts,[46,62,63] we also attempted solid-solution[51,52] formation to achieve further modulation of phase transition behaviors.

Solid solutions were prepared either mechanochemically or with slow evaporation of solution with equimolar amounts of parent compounds (see Experimental section for details). PXRD and DSC measurements were used to characterize the resulting solids and establish whether mixed phase formation was successful.

Despite the aforementioned structural similarities, our efforts solely yielded a real mixed phase in the cases of K^+ and Cs^+. It was observed that the complexes with K^+ were isomorphous through all variations of molar fractions (Fig. ESI-8†) and demonstrated a decrease in the solid-to-solid phase transition temperature in a nearly linear manner as the amount of hydrogenselenate anion in the structure increases, up to 75%, reaching the same value as neat [18-crown-6·K]$HSeO_4$

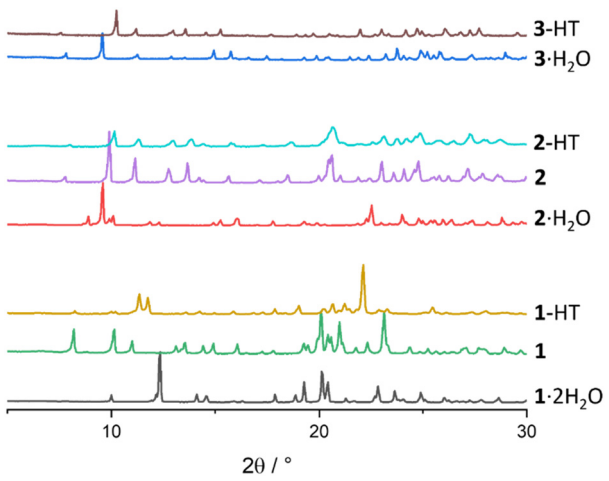

Fig. 3 VT-PXRD patterns recorded at different temperatures for: (**1**·2H_2O), (**2**·H_2O), and (**3**·H_2O).

Table 2 Phase transition temperatures of neat solid acids ($MHSeO_4$, M^+ = K^+, Rb^+, and Cs^+) and their complex with 18-crown-6, as well as those of the formerly reported hydrogensulfate counterparts

M^+	$MHSeO_4$	[18-crown-6·M]$HSeO_4$	[18-crown-6·M]HSO_4
K^+	142 °C (ref. 44)	96 °C	116 °C (ref. 62)
Rb^+	174 °C (ref. 35)	125 °C	116, 122 °C (ref. 46)
Cs^+	127 °C (ref. 35)	86 °C	90 °C (ref. 63)

(Fig. 4 and ESI-9†). Furthermore, the VT-PXRD results show that the solid solutions are also isomorphous to the high-temperature phases of the parent compounds (Fig. ESI-10†).

Powder X-ray diffraction results revealed that the solid solutions of Cs-complexes formed by up to 50% hydrogensulfate crystallized as the [18-crown-6·Cs]$HSeO_4$·H_2O structure. At RT, the solid solutions of [18-crown-6·Cs]$(HSeO_4)_x(HSO_4)_{1-x}$, where $x \geq 0.5$, were all isomorphous (Fig. ESI-11†). The dehydration and phase transition processes were convoluted for all three compounds examined in this range and they all behaved the same which is shown by VT-PXRD and DSC (Fig. ESI-12 and ESI-13†). Increasing the hydrogen sulfate content by more than 50% in the structure caused a physical mixture of parent compounds that is monitored by PXRD at RT and high temperatures (Fig. ESI-11 and ESI-14†). Due to the concurrent nature of the dehydration and order–disorder phase transition processes, we were unable to conduct a detailed analysis of the shift in phase transition temperature.

The attempts made for Rb^+ resulted in physical mixtures, likely due to their subtle structural differences in the hydrated/anhydrous forms, as evidenced by the DSC traces which showed the presence of endothermic peaks attributable to transitions of the respective parent compounds. In Fig. ESI-15,† we can see two endothermic peaks from the hydrogensulfate analogous of Rb^+ and one from the hydrogenselenate. This clearly indicates the formation of a physical mixture.

The overall results agree with the structural considerations, crystalline [18-crown-6·K]$HSeO_4$ and [18-crown-6·K]HSO_4 are

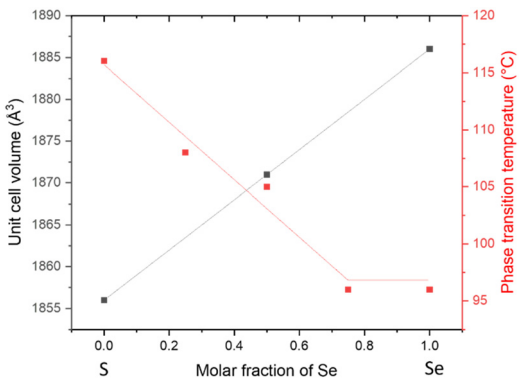

Fig. 4 The trends of unit cell volume and the phase transition temperature *vs.* anion composition of the supramolecular solid solutions [18-crown-6·K]$(HSeO_4)_x(HSO_4)_{1-x}$.

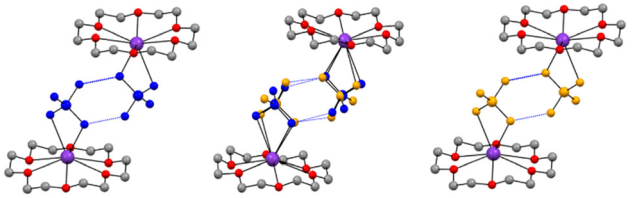

Fig. 5 Crystal structures of [18-crown-6·K]HSO_4 (left), [18-crown-6·K]$(HSeO_4)_{0.5}(HSO_4)_{0.5}$ (middle), and [18-crown-6·K]$HSeO_4$ (right). $HSeO_4^-$ and HSO_4^- depicted in orange and blue respectively, H-atoms omitted for clarity.

highly isomorphous and isostructural at each level (meant as hydrated, anhydrous, and high temperature phases), and the difference in size between the two anions is small (*ca.* 10%).

To further prove solid solution formation, SCXRD analyses were carried out on single crystal specimens grown for the anhydrous hydrogen selenate complex [18-crown-6·K]$HSeO_4$ (**1**) and the mixed-phase obtained with equimolar amounts of anions, [18-crown-6·K]$(HSeO_4)_{0.5}(HSO_4)_{0.5}$ and comparing the unit cell metrics with those of the anhydrous [18-crown-6·K]$HSeO_4$ complex. Fig. 5 showcases the anhydrous structures of [18-crown-6·K]HSO_4,[46] [18-crown-6·K]$HSeO_4$, and their solid solution [18-crown-6·K]$(HSO_4)_{0.5}(HSeO_4)_{0.5}$, (see Table ESI-2† for metal coordination geometries and hydrogen bonding interaction distances). All three structures are isomorphous and isostructural, as mentioned above, and crystallize in the monoclinic $P2_1/n$ space group (see Table ESI-1† for crystallographic details). Notably, the solid solution's unit cell volume satisfies Vegard's rule[64] by lying in the middle of the two parent compounds (Fig. 4) as well as the solid-to-solid transition temperature. In general, the linear response of the unit cell metrics and of physical properties with composition is typical of inorganic alloys but can be extended also to molecular materials.[65]

Conclusions

This study explores the impact of the hydrogen selenate anion, $HSeO_4^-$, in conjunction with various cations (Cs^+, Rb^+, and K^+) that are encapsulated within the cavity of 18-crown-6 ether through coordination interactions on structural arrangements and phase change characteristics of the resulting supramolecular complexes. Single crystals of [18-crown-6·K]$HSeO_4{\cdot}2H_2O$, [18-crown-6·Rb]$HSeO_4{\cdot}H_2O$, and [18-crown-6·Cs]$HSeO_4{\cdot}H_2O$ were grown, and their structures were elucidated through single-crystal X-ray diffraction analysis. The investigation also looked into their dehydration processes and phase transition behaviors using the differential scanning calorimetry (DSC) technique, with subsequent validation and analysis provided by variable-temperature powder X-ray diffraction.

Notably, the inclusion of 18-crown-6 ether into the hydrogenselenates alkali structures resulted in ca 40 °C drop in the solid-to-solid phase transition temperatures compared to the neat solid acids, and at the same time, replacing HSO_4^- with $HSeO_4^-$ induced a decrease of the same phase transition temperature of the anhydrous complexes in the series of ca 20 °C, while significantly altering the behavior of the Rb-complex. The two successive first-order phase transitions previously detected in [18-crown-6·Rb]HSO_4 (ref. 46) turned into one isostructural phase transition.

Additionally, during the same study, we also explored the possibility of obtaining solid solutions between the novel $HSeO_4^-$ supramolecular complexes synthesized in this study and the formerly reported HSO_4^- counterparts.[46,62,63] Attempts made in the case of Rb^+ resulted in physical mixtures, whereas for Cs^+ and K^+ solid solutions [18-crown-6·Cs]$(HSeO_4)_x(HSO_4)_{1-x}$ with $x \geq 0.5$ and [18-crown-6·K]$(HSeO_4)_x(HSO_4)_{1-x}$ with x covering the entire compositional range were obtained. Only for latter, a modulated phase transition temperature was detected, indicating that this is a viable route to achieve fine tuning.

However, it should be stressed that all the anhydrous complexes in the series quickly uptake water from the moisture, posing a challenge to the electrochemical impedance measurements (EIS). Further research is ongoing to stabilize the anhydrous phases and study the ion conduction features of such materials, as well as to extend the same synthetic approach to other systems, and explore how the ions' structural diversity and size may affect the formation of solid solutions and phase transitions in terms of temperature and type.

Data availability

CCDC 2350122–2350126 contain the supplementary crystallographic data for this paper. These data can be obtained free of charge from The Cambridge Crystallographic Data Centre *via* **https://www.ccdc.cam.ac.uk/structures**. The datasets supporting this article have been uploaded as part of the supplementary material.

Author contributions

SD, DB: conceptualization, manuscript preparation; and supervision; SO: experimentation and data collection.

Conflicts of interest

There are no conflicts to declare.

Acknowledgements

SO, DB, and SD thank the University of Bologna (RFO-Scheme) for financial support and the Ms Student Grega Venturini for helping with some synthesis. SD also acknowledges Italian MUR (Fondi PNRR-CNMS-Spoke 13-MOST Code: CN00000023) for financial support.

References

1 B. Hilczer, C. Pawlaczyk and F. E. Salman, *Ferroelectrics*, 1988, **81**, 193–196.
2 D. A. Boysen, T. Uda, C. R. I. Chisholm and S. M. Haile, *Science*, 2004, **303**, 68–70.

3 S. M. Haile, K. D. Kreuer and J. Maier, *Acta Crystallogr., Sect. B: Struct. Sci.*, 1995, **B51**, 680–687.
4 V. V. Sinitsyn, A. I. Baranov and E. G. Ponyatovsky, *Solid State Ionics*, 2000, **136**, 167–171.
5 L. S. Wang, S. V. Patel, S. S. Sanghvi, Y. Y. Hu and S. M. Haile, *J. Am. Chem. Soc.*, 2020, **142**, 19992–20001.
6 L. Fan, Z. Tu and S. H. Chan, *Energy Rep.*, 2021, **7**, 8421–8446.
7 M. Zeng, W. Liu, H. Guo, T. Li, Q. Li, C. Zhao, X. Li and H. Li, *ACS Appl. Energy Mater.*, 2022, **5**, 9058–9069.
8 H. Tang, J. Li, Z. Wang, H. Zhang, M. Pan and S. P. Jiang, *ACS Symp. Ser.*, 2013, **1140**, 243–263.
9 A. Kusoglu and A. Z. Weber, *Chem. Rev.*, 2017, **117**, 987–1104.
10 Y. Sonef, P. Ekdunge and D. Simonsson, *J. Electrochem. Soc.*, 1996, **143**, 1254–1259.
11 H. Gao and K. Lian, *RSC Adv.*, 2014, **4**, 33091–33113.
12 T. Yamada, M. Sadakiyo and H. Kitagawa, *J. Am. Chem. Soc.*, 2009, **131**, 3144–3145.
13 M. Schuster, W. H. Meyer, G. Wegner, H. G. Herz, M. Ise, K. D. Kreuer and J. Maier, *Solid State Ionics*, 2001, **145**, 85–92.
14 G. H. Li, C. H. Lee, Y. M. Lee and C. G. Cho, *Solid State Ionics*, 2006, **177**, 1083–1090.
15 B. Karadedeli, A. Bozkurt and A. Baykal, *Phys. B*, 2005, **364**, 279–284.
16 P. Jhariat, P. Kumari and T. Panda, *CrystEngComm*, 2020, **22**, 6425–6443.
17 T. Kajita, H. Tanaka, Y. Ohtsuka, T. Orido, A. Takano, H. Iwamoto, A. Mufundirwa, H. Imai and A. Noro, *ACS Omega*, 2023, **8**, 1121–1130.
18 S. Ocak, F. Poli, D. Braga, T. Salzillo, F. Tarterini, G. Carì, E. Venuti, F. Soavi and S. d'Agostino, *Cryst. Growth Des.*, 2023, **23**, 4336–4345.
19 Z. Zheng, M. Li, Q. Zhou, L. Cai, J. F. Yin, Y. Cao and P. Yin, *ACS Appl. Nano Mater.*, 2021, **4**, 811–819.
20 M. Rautenberg, B. Bhattacharya, C. Das and F. Emmerling, *Inorg. Chem.*, 2022, **61**, 10801–10809.
21 N. Ma, N. Horike, L. Lombardo, S. Kosasang, K. Kageyama, C. Thanaphatkosol, K. Kongpatpanich, K. I. Otake and S. Horike, *J. Am. Chem. Soc.*, 2022, **144**, 18619–18628.
22 Z. Yang, P. Chen, W. Hao, Z. Xie, Y. Feng, G. Xing and L. Chen, *Chem. – Eur. J.*, 2021, **27**, 3817–3822.
23 Y. Y. Enakieva, A. A. Sinelshchikova, M. S. Grigoriev, V. V. Chernyshev, K. A. Kovalenko, I. A. Stenina, A. B. Yaroslavtsev, Y. G. Gorbunova and A. Y. Tsivadze, *Chem. – Eur. J.*, 2019, **25**, 10552–10556.
24 X. Meng, H. N. Wang, S. Y. Song and H. J. Zhang, *Chem. Soc. Rev.*, 2017, **46**, 464–480.
25 M. T. Caldes, K. V. Kravchyk, M. Benamira, N. Besnard, V. Gunes, O. Bohnke and O. Joubert, *Chem. Mater.*, 2012, **24**, 4641–4646.
26 P. Winiarz, K. Dzierzgowski, A. Mielewczyk-Gryń, M. Gazda and S. Wachowski, *Chem. – Eur. J.*, 2021, **27**, 5393–5398.
27 S. M. Ahn, J. E. Park, G. Y. Jang, H. Y. Jeong, D. M. Yu, J. K. Jang, J. C. Lee, Y. H. Cho and T. H. Kim, *ACS Energy Lett.*, 2022, **7**, 4427–4435.
28 T. Scholz, C. Schneider, M. W. Terban, Z. Deng, R. Eger, M. Etter, R. E. Dinnebier, P. Canepa and B. V. Lotsch, *ACS Energy Lett.*, 2022, **7**, 1403–1411.
29 S. C. Pal, D. Mukherjee, R. Sahoo, S. Mondal and M. C. Das, *ACS Energy Lett.*, 2021, **6**, 4431–4453.
30 R. Sahoo, S. C. Pal and M. C. Das, *ACS Energy Lett.*, 2022, **7**, 4490–4500.
31 J. Luo, O. Conrad and I. F. J. Vankelecom, *J. Mater. Chem. A*, 2013, **1**, 2238–2247.
32 D. B. Shinde, H. B. Aiyappa, M. Bhadra, B. P. Biswal, P. Wadge, S. Kandambeth, B. Garai, T. Kundu, S. Kurungot and R. Banerjee, *J. Mater. Chem. A*, 2016, **4**, 2682–2690.
33 S. M. Haile, *Mater. Today*, 2003, **1369**, 24–29.
34 A. B. Papandrew, C. R. I. Chisholm, R. A. Elgammal, M. M. Özer and S. K. Zecevic, *Chem. Mater.*, 2011, **23**, 1659–1667.
35 A. V. Belushkint, C. J. Carlile and L. A. Shuvalov, *Ferroelectrics*, 1995, **167**, 21–31.
36 A. V. Belushkint, C. J. Carlilet and L. A. Shuvalov, *J. Phys.: Condens. Matter*, 1992, **4**, 389–398.
37 M. Friesel, B. Baranowski and A. Lunden, *Solid State Ionics*, 1989, **35**, 85–89.
38 Z. Hassanzadeh Fard, N. E. Wong, C. D. Malliakas, P. Ramaswamy, J. M. Taylor, K. Otsubo and G. K. H. Shimizu, *Chem. Mater.*, 2018, **30**, 314–318.
39 A. Ikeda, D. A. Kitchaev and S. M. Haile, *J. Mater. Chem. A*, 2014, **2**, 204–214.
40 Y. Matsuda, M. Yonemura, H. Koga, C. Pitteloud, M. Nagao, M. Hirayama and R. Kanno, *J. Mater. Chem. A*, 2013, **1**, 15544–15551.
41 C. Dreßler, G. Kabbe and D. Sebastiani, *J. Phys. Chem. C*, 2016, **120**, 19913–19922.
42 R. B. Merle, C. R. I. Chisholm, D. A. Boysen and S. M. Haile, *Energy Fuels*, 2003, **17**, 210–215.
43 K. D. Kreuer, Th. Dippel, N. G. Hainovsky and J. Maier, *Ber. Bunsenges. Phys. Chem.*, 1992, **96**, 1736–1742.
44 A. Pawłowski and M. Połomska, *Solid State Ionics*, 2005, **176**, 2045–2051.
45 D. A. Boysen, T. Uda, C. R. I. Chisholm and S. M. Haile, *Science*, 2004, **303**, 68–70.
46 S. Ocak, S. d'Agostino, G. Venturini, F. Soavi, S. Bordignon, M. R. Chierotti and D. Braga, *J. Phys. Chem. C*, 2024, **128**, 4789–4795.
47 O. Checa, R. A. Vargas and J. E. Diosa, *Ionics*, 2014, **20**, 545–550.
48 D. Braga, F. Grepioni, L. Maini and S. D'Agostino, *IUCrJ*, 2017, **4**, 369–379.
49 O. Shemchuk, S. D'Agostino, C. Fiore, V. Sambri, S. Zannoli, F. Grepioni and D. Braga, *Cryst. Growth Des.*, 2020, **20**, 6796–6803.
50 D. Braga, *Chem. Commun.*, 2023, **59**, 14052–14062.
51 M. Lusi, *CrystEngComm*, 2018, **20**, 7042–7052.
52 M. Lusi, *Cryst. Growth Des.*, 2018, **18**, 3704–3712.
53 S. D'Agostino, L. Fornasari, F. Grepioni, D. Braga, F. Rossi, M. R. Chierotti and R. Gobetto, *Chem. – Eur. J.*, 2018, **24**, 15059–15066.

54 S. D'Agostino, L. Fornasari and D. Braga, *Cryst. Growth Des.*, 2019, **19**, 6266–6273.
55 S. Ocak, R. Birolo, G. Carì, S. Bordignon, M. R. Chierotti, D. Braga, R. Gobetto, T. Salzillo, E. Venuti, O. Yaffe and S. d'Agostino, *Mol. Syst. Des. Eng.*, 2022, **7**, 950–962.
56 C.-C. Liou and J. S. Brodbelt, *J. Am. Soc. Mass Spectrom.*, 1992, **3**, 543–548.
57 K. Frensdorff, *J. Am. Chem. Soc.*, 1967, **89**, 600–606.
58 G. M. Sheldrick, *Acta Crystallogr., Sect. A: Found. Adv.*, 2015, **71**, 3–8.
59 G. M. Sheldrick, *Acta Crystallogr., Sect. C: Struct. Chem.*, 2015, **71**, 3–8.
60 O. V. Dolomanov, L. J. Bourhis, R. J. Gildea, J. A. K. Howard and H. Puschmann, *J. Appl. Crystallogr.*, 2009, **42**, 339–341.
61 A. Thorn, B. Dittrich and G. M. Sheldrick, *Acta Crystallogr., Sect. A: Found. Crystallogr.*, 2012, **68**, 448–451.
62 D. Braga, M. Gandolfi, M. Lusi, D. Paolucci, M. Polito, K. Rubini and F. Grepioni, *Chem. – Eur. J.*, 2007, **13**, 5249–5255.
63 D. Braga, E. Modena, M. Polito, K. Rubini and F. Grepioni, *New J. Chem.*, 2008, **32**, 1718–1724.
64 A. Denton and N. Ashcroft, *Phys. Rev. A: At., Mol., Opt. Phys.*, 1991, **43**, 3161–3164.
65 A. I. Kitaigorodsky, *Mixed Crystals*, Springer, 1984, vol. 33, pp. 75–81.

